High-density Switchable Skyrmion-like Polar Nanodomains Integrated on Silicon

Lu Han[1,2], Christopher Addiego[3], Sergei Prokhorenko[4], Meiyu Wang[1,2], Hanyu Fu[1,2], Yousra Nahas[4], Xingxu Yan[5,6], Songhua Cai[1,2], Tianqi Wei[1,2], Yanhan Fang[1,2], Huazhan Liu[1,2], Dianxiang Ji[1,2], Wei Guo[1,2], Zhengbin Gu[1,2], Yurong Yang[1,2], Peng Wang[1,2], Laurent Bellaiche[4], Yanfeng Chen[1,2], Di Wu[1,2*], Yuefeng Nie[1,2*], Xiaoqing Pan[3,5,6]

[1]National Laboratory of Solid State Microstructures, Jiangsu Key Laboratory of Artificial Functional Materials, College of Engineering and Applied Sciences, Nanjing University, Nanjing 210093, P. R. China.

[2]Collaborative Innovation Center of Advanced Microstructures, Nanjing University, Nanjing 210093, P. R. China.

[3]Department of Physics and Astronomy, University of California, Irvine, CA 92697, USA.

[4]Physics Department and Institute for Nanoscience and Engineering, University of Arkansas, Fayetteville, AR, USA

[5]Department of Materials Science and Engineering, University of California, Irvine, CA 92697, USA.

[6]Irvine Materials Research Institute, University of California, Irvine, CA 92697, USA.

*Correspondence to: diwu@nju.edu.cn, ynie@nju.edu.cn

Topological domains in ferroelectrics have received much attention recently due to their novel functionalities and potential applications in electronic devices. To date, however, such topological polar structures were only observed in superlattices grown on oxide substrates, limiting their applications in silicon-based electronics. Here, we report the realization of room-temperature skyrmion-like polar nanodomains in $PbTiO_3/SrTiO_3$ bilayers transferred on silicon. Moreover, an external electric field can reversibly switch these polar nanodomains into another type of polar texture, which substantially modifies their resistive behaviors. The polar-configuration-modulated resistance is ascribed to the distinct band bending and charge carrier distribution in the core of two different types of polar textures. The integration of high-density (>200 Gbit/inch^2) switchable skyrmion-like polar nanodomains on silicon paves the way toward non-volatile memory applications using topological polar structures in oxides.

Recent discoveries have shown, at all scales, that ferroelectric polarization can form complex topological structures, such as flux-closure domains[1-4], vortices[5-12], non-Ising-like domain walls[13,14], labyrinthine domains[15,16], bubbles[17], incommensurate curl domains[18], polar skyrmions[19,20], merons[21,22], and others[23]. Owing to the polarization and charge distribution discontinuity, the nonuniform polar textures could give rise to emergent functionalities distinct from the bulk domains, including electric conductivity[24,25], dielectric response[26], piezoelectricity[27], thermal resistance[28] and negative capacitive response[29,30]. These emergent functionalities hold the potential for novel applications in next-generation electronic devices. For instance, an array of nanometer-size polar skyrmions, if they can be read and written easily, will be promising for ultrahigh-density recording well above Tbit/inch^2 [11,12]. Despite these rich physical properties and promising potential applications, it is still rather challenging to integrate these topological textures into silicon-based technology since they are mostly observed in superlattices grown on single crystal oxide substrates.

Here, we demonstrate the observation of high-density (~200 Gbit/inch^2) skyrmion-like polar nanodomains in freestanding $(PbTiO_3)_{20}/(SrTiO_3)_{10}$ bilayers transferred on silicon. These topological nanodomains are switchable under external electric field. The resistance of these polar nanodomains is greatly modulated by reversibly switching between two different types of polarization structures, providing a new route to design non-volatile ferroelectric memories using topological polar structures.

A series of $(PbTiO_3)_m/(SrTiO_3)_n$ (m, n: number of unit cells) bilayers were grown on $SrTiO_3$ (001) substrates using water-soluble $Sr_3Al_2O_6$ (SAO) as the sacrificial layer[31-35] by reactive molecular beam epitaxy (MBE). The bilayers were then released by dissolving the SAO buffer layer in deionized water and laminated on a platinized Si (001) substrate (Fig. 1a). More details about the film growth, transfer and characterizations can be found in the Materials and Methods section, Extended Data Fig. 1 and Extended Data Fig. 2 in the Supplementary Materials.

Domain structures of the ferroelectric/paraelectric bilayers were characterized by vector piezoelectric force microscope (PFM)[10,36], a technique to extract three-dimensional polarization information by simultaneous mapping vertical and lateral piezo-response signals. The pristine state of a $(PbTiO_3)_{20}/(SrTiO_3)_{10}$ exhibits two types of round-shape nanodomains highlighted by red and blue circles (Fig. 1b) and their zoom-in PFM images are shown in Fig. 1c and Fig. 1d, respectively. Interestingly, these polar textures are not directly related to the topography of the samples. For the red-circled nanodomains, the vertical PFM (VPFM) amplitude image shows a ring-shape dark contrast and the phase image shows a 180° phase inversion between the out-of-plane polarization at the center and that in the surrounding background region. The lateral PFM (LPFM) phase image shows a half-violet and half-yellow contrast and the amplitude image shows round-shape bright contrast split by a dark line, indicating a phase inversion of the lateral polarization component along the direction perpendicular to the cantilever. Since the lateral PFM technique relies on the torsional vibration mode of the cantilever, only the polarization component projected to the in-plane axis perpendicular to the cantilever is distinguished (Extended Data Fig. 3a). In other words, if the cantilever is parallel to the y axis, LPFM only measures the polarization component along the x axis. At the region with zero x components, there is no torsional vibration. By rotating the sample clockwise for a set of given angles (Fig. 2a), the dark line in the LPFM amplitude image rotates continuously with the cantilever and the phase image always shows a 180° phase inversion of the polarizations between the left and right side of the cantilever, implying that the in-plane polarization has a rotation symmetry about the center of the nanodomains. Following the method proposed in previous works[10,36], our in-plane vector PFM mapping shows that the red-circled nanodomains have a center-divergent pattern (Fig. 2b). Then we calculated the divergence using the vector PFM image shown in Fig. 2b (Extended Data Fig. 4c), which enables us to distinguish the center-divergent domains between the four-domain vortices (Extended Data Fig. 4a) and skyrmion-like bubbles (Extended Data Fig. 4b). Combining the out-of-plane and in-plane polarization information, three-dimensional polar textures of the red-circled nanodomains are depicted schematically in Fig. 1c, indicating that these red-circled nanodomains are Néel-type skyrmion-like nanodomains. (More details about the vector PFM mapping can be found in Materials and Methods section and Extended Data Fig. 3 in Supplementary Materials)

In contrast, the blue-circled nanodomains exhibit no inversion of the out-of-plane polarizations and their in-plane polarizations show a center-convergent pattern (Fig. 1d, Fig. 2a and Fig. 2b), indicating that they are not Néel-type skyrmions. As will be shown later, these blue-circled (center-convergent) nanodomains are closely related to the center-divergent nanodomains but show different resistive behaviors. Interestingly, throughout the PFM measurements, both types of nanodomains display a central symmetry and are quite stable, which are essential for further manipulation and application as a functional unit in devices.

To confirm that the polar textures observed in PFM measurements are indeed topological structures, we also performed polarization mapping on our PTO/STO bilayer samples using 4D scanning transmission electron microscopy (4D-STEM) using a nanoscale electron probe. The polarization in ferroelectric materials can be determined from convergent beam diffraction (CBED) patterns based on the difference in intensity distribution between conjugate pair diffraction disks. This technique has been used to investigate the polarization configuration in many other intriguing ferroelectric systems, including ferroelectric domains in $BaTiO_3$[37], polar vortices in PTO/STO superlattice[38], and polar skyrmions in STO/PTO/STO tri-layers[20]. Our 4D-STEM results confirm both the center-divergent-type (Figs. 2c & 2d) and the center-convergent-type polar nanodomains (Extended Data Fig. 5a). The typical size (about 5-9 nm) of the skyrmion-like nanodomains is smaller than that observed in the PFM measurements, which may be related to the resolution of the PFM technique limited by the tip size (Extended Data Fig. 6)[39,40]. Also note that these polar nanodomains are unlikely driven by extrinsic effects[41,42] since no clear lattice and charged defects have been detected in HAADF-STEM (Extended Data Fig. 7a), position averaged convergent beam electron diffraction (PACBED) (Extended Data Fig. 7b) and charge density maps (Extended Data Figs. 5b & 5c).

The stabilization of such polar skyrmion-like nanodomains in $PbTiO_3/SrTiO_3$ bilayer is supported by our effective Hamiltonian model simulations[43,44], an *ab initio* method employed in studying many ferroelectric vortices and other topological textures[11,16] (More details about the simulations are available in Materials and Methods section). As shown in Fig. 3, the simulated freestanding bilayer structure corresponds to round-shaped down-oriented nanodomains with a diameter of 10-15 unit cells (5 to 7 nm) embedded in an upwards-polarized matrix, consistent with the size observed in 4D-STEM data. In accordance with experimental observations, we also find that the in-plane polarization within such nanodomains features center-divergent character (Fig. 3a) with the two-dimensional winding number[45] equal to one for each domain. The origin of this non-trivial in-plane topology can be traced back to asymmetric screening conditions for the PTO layer[46]. Namely, the poor screening of bound charges at the PTO/STO interface induces Néel polarization rotation in planes passing through the axis perpendicular to the interface. As a result, the nano-domain boundary has a rounded closure in the vicinity of STO layer that does not reach the STO surface (Figs. 3b, 3c & 3d). Within the first unit-cell layer of PTO above the STO surface, the dipoles are aligned along the polarization of the embedding matrix, but also feature a center-divergent pattern formed by in-plane dipolar components. The second layer above the STO surface reveals a classical Néel skyrmion pattern with down-wards oriented core (Figs. 3c & 3d) at the tip of the nanodomain boundary. Moving further away from the interface, the core of the nanodomain first enlarges and the Néel rotations disappear 6 layers above the interface, leading to a sharp 180° circular domain wall boundary of fixed radius. At the free PTO interface, the dipoles are aligned perpendicular to the surface because of the ideal electrostatic screening conditions. More details about the topological characterization of skyrmion-like nanodomains can be found in the Materials and Methods section, Extended Data Fig. 8 and Extended Data Fig. 9 in the Supplementary Materials.

Interestingly, our effective Hamiltonian model simulations indicate that another state can be also stabilized by only switching the top part of the dipoles from pointing downwards to upwards as the surrounding background (Fig. 2e), which explains the observation of center-convergent nanodomains. As shown in Extended Data Fig. 10, above and below the resulting Néel bubble skyrmion[17,47,48], the local dipoles lean towards and away from the central revolution axis, respectively. However, the center-divergent distortion below the domain is not fully developed because of the STO layer. As a result, in accordance with our PFM and 4D-STEM experiments, the local polarization averaged over the bilayer thickness has a center-convergent character.

The stability of Néel skyrmion-like polar nanodomains crucially depends on the thickness of PTO and STO layers. The STO layer is essential to create strong depolarizing field at the origin of non-trivial dipolar rotations. Moreover, it elastically constrains the PTO layer and gives rise to a built-in field, both of which prevent development of in-plane oriented tetragonal domains while also breaking the remaining Z_2 tetragonal symmetry[47]. The stabilization of skyrmion-like polar nanodomains is subject to a delicate balance of these factors that can be changed by tuning the volume fraction of PTO. For instance, considering the STO thickness fixed and decreasing the number of PTO layers gives rise to two competing mechanisms. The first one is related to a drop of the coercive field magnitude, and consequently, a more pronounced role of the built-in field. Such mechanism favors homogeneously polarized state. The competing mechanism is related to enhanced in-plane clamping of PTO upon increasing the STO volume fraction which, inversely, increases the transition temperature and coercive field magnitude.

The importance of PTO layer thickness as the parameter governing stability of skyrmion-like polar nanodomains is consistent with our experimental observations that skyrmion-like textures only exist in $(PbTiO_3)_{20}/(SrTiO_3)_{10}$ films among $(PbTiO_3)_n/(SrTiO_3)_{10}$ (n = 12, 16, 20) bilayers (Extended Data Fig. 11). Indeed, the x-ray diffraction (XRD) images indicate a sharp change of the lattice parameters of the 20 u.c. freestanding $PbTiO_3$ film with or without 10 u.c. $SrTiO_3$ layer (Extended Data Fig. 12). After transfer, the polarization in the $PbTiO_3$ layer has a tendency to rotate from the out-of-plane direction to the in-plane direction due to the strong depolarization field, thus increasing the in-plane lattice parameter of $PbTiO_3$. So, the $SrTiO_3$ layer will introduce an elastic constraint to the $PbTiO_3$. This exact elastic constraint value can be varied by manipulating the thickness ratio of these two layers ($z = t_{PTO}/t_{STO}$) to tune the competition between the elastic energy of these two layers. The significant reduction of the tetragonality (from 1.04 to 1.01) by adding the dielectric $SrTiO_3$ layer provides a suitable situation where skyrmion-like nanodomains can exist.

It is of great interest to explore whether the skyrmion-like polar nanodomains are tunable and how these two types of nanodomains will respond to external electric field stimuli. To this end, we apply a scanning tip bias of +5 V and -5 V to a 500×250 nm^2 region of a $(PbTiO_3)_{20}/(SrTiO_3)_{10}$

bilayer (Extended Data Fig. 13). The PFM data were taken under an AC amplitude of 500 mV after applying the +5V/-5V DC voltage, which indicates the non-volatile switching behavior of these nanodomains. Remarkably, only the center-divergent (center-convergent) type of nanodomains are observed after scanning with positive (negative) bias, indicating these two types of nanodomains can be reversibly switched to their counterparts by an external electric field. The reversible switching between these two types of nanodomains indicates they are closely related to each other as revealed in the PFM, 4D-STEM and effective Hamiltonian model simulations. Ideally, two equivalent Néel-type skyrmion-like states should be stabilized by simply reversing the polarization of each electric dipole if the material system is symmetric. However, consistent with our computational simulations, there is inherent inversion symmetry breaking in the PTO/STO bilayer along the out-of-plane direction, giving rise to an upwards background polarization most likely due to the existence of a built-in electric field at the interface[49]. Due to this built-in electric field, the external electric field applied by the tip can only reverse part of the dipoles and convert these two types of nanodomains reversibly. We also transferred the freestanding bilayer on P-doped silicon substrate and etched the film into quadrate patterns via a standard electron beam lithography process. As shown in Extended Data Fig. 14, the topological nanodomains still exist, which indicates the freestanding film and skyrmion-like nanodomains can be integrated with silicon and survive typical processing steps used in silicon device fabrication.

To explore the potential application in resistive memories, we also investigated the resistive behaviors of these topological nanodomains using conductive atomic force microscopy (CAFM) as shown in Fig. 4. The measured current in the core of center-convergent polar nanodomains is similar to the insulating surrounding background area, making this type of topological domains indistinguishable from the matrix. Strikingly, for center-divergent polar nanodomains, the core shows a two orders of magnitude enhancement of the conductivity, with a current up to 10^2 pA at 5 V bias. Also, these distinct resistive states can be reversibly switched by applying electric field to switch between two types of polar nanodomains. As shown in Fig. 4b, after writing polar nanodomains on the bilayer by applying +5 V bias on the tip, high density round-shape nanodots with a high current value are observed in the current map. After switching the center-divergent polar nanodomains to center-convergent nanodomains by a scan with -5 V bias, the round-shape high current nanodots disappear. Due to the existence of an insulating $SrTiO_3$ layer (~ 4 nm), we need relatively high voltages (+5 V/-5 V bias voltage) to tunnel the energy barrier in order to obtain low noise data when measuring the current maps, which could switch the polar nanodomains and alter the original information (Extended Data Fig. 15). Nonetheless, the current maps of these two different domains exhibit different resistive states (Fig. 4b). Presently, PFM and STEM are the techniques to read the non-volatile information. In order to obtain reliable non-destructive reading of the resistive states, lowering the tunneling voltage by reducing the thickness of the STO layer while maintaining skyrmion-like nanodomains is a possible solution. Using other techniques which can measure the resistive states without applying high external DC voltage may also be helpful. This reversible switching of the nanodomain types and resistive states provides a new route to design resistive memory devices based on topological polar nanodomains.[50]

The possible mechanism to explain the observed phenomena is schematically shown in Fig. 4c. The ferroelectric PTO and paraelectric STO bilayer sandwiched by the bottom electrode and the conducting tip forms a junction and its resistance can be tuned if the polar skyrmion-like nanodomains can be switched between insulating and conducting states. Similar to the highly conducting channels observed in the ferroelectric domain walls[10,24,51,52], it is not surprising to expect enhanced conductivity in the vicinity of the core of center-divergent nanodomains since there is such a large polarization divergence. In contrast, due to the absence of inversion of the out-of-plane polarization in the center-convergent nanodomains, the polarization divergence near its core is lower since the electric dipoles do not need to experience the fully in-plane orientation to bridge the antiparallel orientations at the core and surrounding background. As such, two different types of nanodomains lead to different barrier widths and band diagrams of the junction, giving rise to distinct resistive states (Fig. 4c). As shown in our PFM, 4D-STEM and computational simulations, the lateral size of polar nanodomains are ~30 nm or smaller, corresponding to a pixel density of ~200 Gbit/inch^2 or higher, which is higher than that in commercialized memory devices and the artificially-synthesized array of ferroelectric nanodots[8,53].

In summary, we report the observation of two-types (center-divergent and center-convergent types) of skyrmion-like polar nanodomains in $PbTiO_3/SrTiO_3$ bilayers transferred on silicon. These two types of nanodomains can be converted to each other by applying an external electric field. High density resistive memories based on these topological nanodomains have been demonstrated and the “on” and “off” states can be controlled by switching the type of polar nanodomains. There are several unique advantages of this type of polar textures integrated on silicon: 1) Since there is only a single layer of skyrmion-like nanodomains instead of multiple layers of interacting skymions, it is easier to switch each individual skyrmion-like nanodomain by external electric field, allowing the effectively “write” operation. Also, without the interference between multilayers of skyrmion-like nanodomains, it also enables the direct mapping of the polarization patterns by PFM measurements, which is actually a non-destructive “read” operation. 2) As the whole structure is thin enough, the modification of the conductivity of the skyrmion-like nanodomains can effectively tune the resistive state of the bilayer system near the core of the nanodomains, allowing the non-destructive “read” operation. Since it is non-destructive and no need to switch the polarizations, this “read” operation can be much faster than the conventional ferroelectric RAM (FeRAM) where the read process is destructive, necessitating a write-after-read architecture. 3) More importantly, this unique structure can be integrated on silicon wafers. The integration of high-density switchable skyrmion-like polar nanodomains on silicon paves the way toward non-volatile memory applications using topological polar structures in oxides.

METHODS SUMMARY

Sample Growth. Water-soluble $Sr_3Al_2O_6$(SAO) layer was grown first on (001) STO single-crystalline substrate (MTI) followed by the growth of STO and PTO by a DCA Dual R450 Oxide MBE system. The SAO and STO films were grown with an oxidant (10% O_3 and 90% O_2) background pressure p_{O_2} of 1×10^{-6} Torr and at $T_{\mathrm{substrate}} = 950$ °C in a layer-by-layer growth mode, of which the thickness was monitored by RHEED oscillations. The PTO films were grown with an oxidant (distilled O_3) background pressure of 2×10^{-5} Torr and at $T_{\mathrm{substrate}} = 625$ °C. Due to the volatility of lead, PTO films were grown in adsorption-controlled mode with a fixed Pb:Ti flux ratio of 13:1 and the thickness is controlled by shutter time of titanium.

Structure Characterizations. The crystal structure was examined by a high-resolution four-circle X-ray diffractometer using a Bruker D8 Discover instrument. The incident X-ray is from Cu-K_α emission and has a wavelength of 1.5418 Å.

SAED and S/TEM Experiments. SAED patterns were acquired on a FEI Tecnai F20 TEM at 200 kV from a flat area of the samples suspended on holey carbon films or micro carbon grids. Low electron beam current (0.045 nA) and short exposure time (2.0 s) were employed to reduce electron beam damage. The probe convergence angle on Titan was 25 mrad, and the angular range of the HAADF detector was from 79.5 to 200 mrad.

4D-STEM measurements. TEM samples were prepared by transferring freestanding PTO/STO bilayers to a copper grid with holey carbon support. 4D STEM data was collected on a JEOL JEM-ARM300F at 300 kV. CBED patterns were recorded on a Gatan Oneview at 1024×1024 resolution running at 200 fps with 0.5 nm pixel size. A convergence angle of 2.4 mrad was used so that the diffraction disks from the (001) plane were well separated.

To determine the polarization, we used the intensity distribution of conjugate pair diffraction disks (also called Friedel pair disks). When there is no polarization present, the intensity distribution in Friedel pair disks will be symmetric, reflecting the inversion symmetry of the structure. The polarization in PTO breaks this symmetry, so the Friedel pair disks will have an asymmetric intensity distribution. We quantified the asymmetric intensity distribution in each CBED pattern by calculating the center of mass (COM) of each $\{200\}$ family diffraction disk. The COM from (200) and $(\bar{2}00)$ were averaged together and a reference position was calculated as the average of the combined $(200)/(\bar{2}00)$ COM from all CBED patterns in the 4D dataset. The shift in the combined $(200)/(\bar{2}00)$ COM away from the reference point was then taken as the polarization along [100]. The polarization along [010] was calculated analogously from the (020) and $(0\bar{2}0)$ diffraction disks.

Since the samples were imaged from (001), the PTO and STO layers did overlap in projection. However, since STO is unpolarized, its contribution to the COM does not change with position and will be removed by subtracting the reference position.

Piezoresponse Force Microscopy (PFM) Measurements. The local piezoelectric and ferroelectric properties of freestanding films on a platinum-coated silicon wafer were examined using an Asylum Research MFP-3D Origin+ scanning probe microscope. NanoWorld EFM Pt/Ir-coated tips (2.8 N/m in force constant) were used in the PFM measurements. Hysteresis loops were collected in the dual AC resonance tracking (DART) mode[54]. The vector PFM measurements were done by following the method reported previously[10,36] and schematically shown in Extended Data Fig. 3.

Conductive Atomic Force Microscopy (CAFM) Measurements. CAFM experiments were performed with an Asylum ORCA cantilever holder with a gain of 1×10^{-9} V/A. The bias voltage was applied to the sample and the tip was virtually grounded for all measurements. I-V data were collected with a triangular voltage shape (ramp of 3 V/s; 2,000 points/s).

Effective Hamiltonian model simulations. Within our simulations, the PTO layer is described by the effective Hamiltonian model of bulk PTO[55]. The crystalline structure is characterized using the local mode representation of electric dipoles, the displacements of A-site cations parametrizing the inhomogeneous strain in each unit cell and the six-component homogeneous strain tensor[56]. The PTO effective Hamiltonian comprises the 8th order polynominal on-site energy terms, short-range and long-range local mode interactions as well as local mode-strain coupling and the elastic energy. The STO layer is assumed to be a dielectric slab with constant electric permittivity $\epsilon = 10$. Furthermore, we take into account homogeneous deformations of STO. The STO elastic constants are taken to be $\mathrm{b}_{11} = 131.33$ eV, $\mathrm{b}_{12} = 36.26$ eV, and $\mathrm{b}_{12} = 41.3$ eV and the lattice parameter $\mathrm{a}_{STO} = 3.901$ Å[57]. The elastic coupling of STO and PTO layers is introduced by matching the in-plane strain components of the homogeneous strain tensor in PTO and STO layers. At the top and bottom interfaces of the bilayer, we impose ideal screening conditions resulting from either ambient charges or metallic electrodes[58] while the effects of asymmetric chemical pressure at the PTO interfaces are mimicked by an out-of-plane homogeneous electric field. For all simulations we use 64×64×30 supercells with 10 u.c. STO layer and 20 u.c. PTO layer.

Numerically, the pristine bilayer state is obtained through a temperature quench[16,47] with the in-plane lattice constants fixed to $SrTiO_3$ bulk value and bias field of 2×10^8 V/m during which the system is cooled from 800 K down to 300 K with steps of 50 K. (note that electric fields are typically overestimated in effective Hamiltonians, with such overestimation having, e.g., been found to be a factor of 25 in the $BiFeO_3$ material[59].) At each temperature, the structure is relaxed for 5,000 hybrid Monte Carlo sweeps[60]. The resulting room-temperature supercell configuration is then "lifted" from the substrate by removing the constraint of fixed in-plane strain and performing additional 100,000 relaxation sweeps.

Lithography Process on P-doped Silicon Wafer. The ferroelectric bilayer was first transferred onto P-doped silicon wafer via the same method described in Extended Data Fig. 1. After spin coating the sample with 400 nm of PMMA, the quadrate arrays (with a side of 5 μm) were defined using electron beam lithography (EBL) over a 500 μm × 500 μm area. After cold development in MIBK:IPA 1:3, the sample was cleaned with an IPA rinse and dried under an N_2 stream. The PMMA was then used a mask for ionic beam etching (IBE). After that, the PMMA was removed by acetone.

Topological characterization. To characterize the topology of the simulated polar domains, we have computed the skyrmion number N_{Sk} and the distribution of the Pontryagin topological charge density[61] ρ_{Sk} within each (001) u.c. plane of the PTO layer.

The charge density ρ_{Sk} is given by[19]

$$\rho_{Sk} = \frac{1}{4\pi}\vec{n} \cdot (\partial_x\vec{n} \times \partial_y\vec{n}), \qquad (1)$$

where $\vec{n}$ denotes a normalized polarization vector at each point $\vec{R} = (x, y)$ and the skyrmion number is obtained by taking a surface integral of ρ_{Sk}, i.e. $N_{Sk} = \int d\vec{R}\,\rho_{Sk}(\vec{R})$.

Here, we approximate the $\vec{n}$ vector field by a cubic lattice of the Pb-centered, normalized, local mode vectors and a single ρ_{Sk} value is assigned to each unit cell using a lattice analogue of Eq. (1)[62]. To obtain the plane resolved N_{Sk}, we then sum the calculated ρ_{Sk} values over all unit cells comprising a single z=const plane.

For all planes, except the interfacial (z=1) PbO layer, we find that N_{Sk} is a negative integer number, whose absolute value corresponds to the number of center-divergent domains. For the interfacial z=1 PbO layer, we find that N_{Sk} is equal zero.

These results suggest that a single center-divergent polar domain carries a N_{Sk} skyrmion number of -1 in each $z \neq 1$ plane.

To confirm this idea, we now turn to the polar structure and the distribution of the Pontryagin charge density within a single center-divergent domain. The distribution of dipoles within the first three layers above the PTO/STO interface is shown in Extended Data Fig. 8 (a-b). Extended Data Fig. 8b additionally shows the distribution of the calculated ρ_{Sk} values. As it can be seen, the distributions of local dipoles and ρ_{Sk}, feature a quasi-continuous rotational symmetry around the central [001] axis of the domain. Moreover, for $z \geq 2$, the Pontryagin charge density distribution has a ring-like shape with its maximum located at the center of the quasi-circular 180 ° domain wall (See Extended Data Fig. 8b). Notably, similar distribution of ρ_{Sk} is characteristic of the polar bubble skyrmions observed in symmetric STO/PTO/STO heterostructures[20]. However, in our case, we do not observe the Bloch-like rotations of dipoles in the vicinity of the domain wall center[20].

Calculating the skyrmion number $N_{Sk}(R) = 2\pi \int_0^R dr\ r\ \rho_{Sk}$ as a function of the distance from the central domain axis (see Extended Data Fig. 9a) shows that a single center-divergent domain can be indeed associated with an integer skyrmion number $N_{Sk} = -1$.

It is important to note that, as discussed in the manuscript, the interfacial dipolar structure (see Extended Data Fig. 8 and Fig. 3 in the manuscript) of z=2 layer is retained up to $z = 6$. Within this interfacial region ($1 < z < 7$) increasing z leads to an increase of the diameter of the down-oriented domain core and monotonous reduction of the domain wall width. These transformations of the dipolar structure are continuous and bear no incidence on the topology. At $z = 7$, the width of a circular domain wall reduces to ~ 1 u.c. and the diameter of the domain reaches its maximum value that no longer increases with increasing z. For $z \geq 7$, the topological characterization described above still yields $N_{Sk} = -1$ for each z=const plane. However, in the view of ~ 1 u.c. thickness of the domain wall, such characterization loses its physical meaning. Therefore, based on the presented topological characterization results, we can conclude that the center-divergent domains are associated with an interfacial topological soliton akin to Néel magnetic skyrmions. Similar defects, called bobbers, were previously reported in magnetic thin films[63], which have never been found in ferroelectrics before.

Interestingly, similar to magnetic Bobbers, we find that the simulated center divergent domains feature a Bloch point located at the domain tip at z=1.5.

References

1 Balke, N. *et al.* Deterministic control of ferroelastic switching in multiferroic materials. *Nat. Nanotechnol.* **4**, 868 (2009).

2 Ivry, Y., Chu, D. P., Scott, J. F. & Durkan, C. Flux closure vortexlike domain structures in ferroelectric thin films. *Phys. Rev. Lett.* **104**, 207602 (2010).

3 McQuaid, R. G. P., McGilly, L. J., Sharma, P., Gruverman, A. & Gregg, J. M. Mesoscale flux-closure domain formation in single-crystal $BaTiO_3$. *Nat. Commun.* **2**, 404 (2011).

4 Tang, Y. L. *et al.* Observation of a periodic array of flux-closure quadrants in strained ferroelectric $PbTiO_3$ films. *Science* **348**, 547 (2015).

5 Rodriguez, B. J. *et al.* Vortex Polarization States in Nanoscale Ferroelectric Arrays. *Nano Lett.* **9**, 1127 (2009).

6 Chae, S. C. *et al.* Self-organization, condensation, and annihilation of topological vortices and antivortices in a multiferroic. *Proc. Natl. Acad. Sci. U. S. A.* **107**, 21366 (2010).

7 Yadav, A. K. *et al.* Observation of polar vortices in oxide superlattices. *Nature* **530**, 198 (2016).

8 Li, Z. *et al.* High-density array of ferroelectric nanodots with robust and reversibly switchable topological domain states. *Sci. Adv.* **3**, e1700919 (2017).

9 Shafer, P. *et al.* Emergent chirality in the electric polarization texture of titanate superlattices. *Proc. Natl. Acad. Sci. U. S. A.* **115**, 915 (2018).

10 Kim, K. E. *et al.* Configurable topological textures in strain graded ferroelectric nanoplates. *Nat. Commun.* **9**, 403 (2018).

11 Naumov, I. I., Bellaiche, L. & Fu, H. Unusual phase transitions in ferroelectric nanodisks and nanorods. *Nature* **432**, 737 (2004).

12 Stachiotti, M. G. & Sepliarsky, M. Toroidal Ferroelectricity in $PbTiO_3$ Nanoparticles. *Phys. Rev. Lett.* **106**, 137601 (2011).

13 Wei, X. K. *et al.* Neel-like domain walls in ferroelectric $Pb(Zr,Ti)O_3$ single crystals. *Nat. Commun.* **7**, 12385 (2016).

14 De Luca, G. *et al.* Domain Wall Architecture in Tetragonal Ferroelectric Thin Films. *Adv. Mater.* **29**, 1605145 (2017).

15 Eliseev, E. A. *et al.* Labyrinthine domains in ferroelectric nanoparticles: Manifestation of a gradient-induced morphological transition. *Physical Review B* **98**, 054101 (2018).

16 Nahas, Y., Prokhorenko, S., Fischer, J., Xu, B. & Bellaiche, L. Inverse transition of labyrinthine domain patterns in ferroelectric thin films. *Nature* **577**, 47 (2020).

17 Zhang, Q. *et al.* Nanoscale Bubble Domains and Topological Transitions in Ultrathin Ferroelectric Films. *Adv. Mater.* **29**, 1702375 (2017).

18 Peters, J. J. P., Apachitei, G., Beanland, R., Alexe, M. & Sanchez, A. M. Polarization curling and flux closures in multiferroic tunnel junctions. *Nat. Commun.* **7**, 13484 (2016).

19 Nahas, Y. *et al.* Discovery of stable skyrmionic state in ferroelectric nanocomposites. *Nat. Commun.* **6**, 8542 (2015).

20 Das, S. *et al.* Observation of room-temperature polar skyrmions. *Nature* **568**, 368 (2019).

21 Lu, L. *et al.* Topological Defects with Distinct Dipole Configurations in $PbTiO_3/SrTiO_3$ Multilayer Films. *Phys. Rev. Lett.* **120**, 177601 (2018).

22 Wang, Y. J. *et al.* Polar meron lattice in strained oxide ferroelectrics. *Nat. Mater.* **19**, 881 (2020).

23 Prokhorenko, S., Nahas, Y. & Bellaiche, L. Fluctuations and Topological Defects in Proper Ferroelectric Crystals. *Phys. Rev. Lett.* **118**, 147601 (2017).

24 Crassous, A., Sluka, T., Tagantsev, A. K. & Setter, N. Polarization charge as a reconfigurable quasi-dopant in ferroelectric thin films. *Nat. Nanotechnol.* **10**, 614 (2015).

25 Seidel, J. *et al.* Conduction at domain walls in oxide multiferroics. *Nat. Mater.* **8**, 229 (2009).

26 Xu, R., Karthik, J., Damodaran, A. R. & Martin, L. W. Stationary domain wall contribution to enhanced ferroelectric susceptibility. *Nat. Commun.* **5**, 3120 (2014).

27 Wada, S., Yako, K., Yokoo, K., Kakemoto, H. & Tsurumi, T. Domain Wall Engineering in Barium Titanate Single Crystals for Enhanced Piezoelectric Properties. *Ferroelectrics* **334**, 17 (2006).

28 Langenberg, E. *et al.* Ferroelectric Domain Walls in $PbTiO_3$ Are Effective Regulators of Heat Flow at Room Temperature. *Nano Lett.* **19**, 7901 (2019).

29 Zubko, P. *et al.* Negative capacitance in multidomain ferroelectric superlattices. *Nature* **534**, 524 (2016).

30 Das, S. *et al.* Local negative permittivity and topological phase transition in polar skyrmions. *Nat. Mater.* (2020).

31 Lu, D., Crossley, S., Xu, R., Hikita, Y. & Hwang, H. Y. Freestanding Oxide Ferroelectric Tunnel Junction Memories Transferred onto Silicon. *Nano Lett.* **19**, 3999 (2019).

32 Ji, D. *et al.* Freestanding crystalline oxide perovskites down to the monolayer limit. *Nature* **570**, 87 (2019).

33 Dong, G., Li, S., Yao, M., Zhou, Z. & Liu, M. Super-elastic ferroelectric single-crystal membrane with continuous electric dipole rotation. *Science* **366**, 475 (2019).

34 Han, L. *et al.* Giant Uniaxial Strain Ferroelectric Domain Tuning in Freestanding $PbTiO_3$ Films. *Adv. Mater. Inter.* **7**, 1901604 (2020).

35 Hong, S. S., Gu, M., Verma, M., Harbola, V. & Hwang, H. Y. Extreme tensile strain states in $La_{0.7}Ca_{0.3}MnO_3$ membranes. *Science* **368**, 71 (2020).

36 Kim, J., You, M., Kim, K.-E., Chu, K. & Yang, C.-H. Artificial creation and separation of a single vortex–antivortex pair in a ferroelectric flatland. *npj Quantum Mater.* **4**, 29 (2019).

37 Tsuda, K., Yasuhara, A. & Tanaka, M. Two-dimensional mapping of polarizations of rhombohedral nanostructures in the tetragonal phase of $BaTiO_3$ by the combined use of the scanning transmission electron microscopy and convergent-beam electron diffraction methods. *Appl. Phys. Lett.* **103**, 387 (2013).

38 Yadav, A. K. *et al.* Spatially resolved steady-state negative capacitance. *Nature* **565**, 468 (2019).

39 Kalinin, S. V. *et al.* Spatial resolution, information limit, and contrast transfer in piezoresponse force microscopy. *Nanotechnology* **17**, 3400 (2006).

40 Tian, L. *et al.* Nanoscale polarization profile across a 180° ferroelectric domain wall extracted by quantitative piezoelectric force microscopy. *J. Appl. Phys.* **104**, 074110 (2008).

41 Lee, D. *et al.* Emergence of room-temperature ferroelectricity at reduced dimensions. *Science* **349**, 1314 (2015).

42 Kim, S. D., Hwang, G. T., Song, K., Chang, K. J. & Choi, S. Y. Inverse size-dependence of piezoelectricity in single $BaTiO_3$ nanoparticles. *Nano Energy* **58**, 78 (2019).

43 Zhong, W., Vanderbilt, D. & Rabe, K. M. Phase transitions in $BaTiO_3$ from first principles. *Phys. Rev. Lett.* **73**, 1861 (1994).

44 Bellaiche, L., Garcia, A. & Vanderbilt, D. Finite-temperature properties of Pb($Zr_{1-x}Ti_x$)O_3 alloys from first principles. *Phys. Rev. Lett.* **84**, 5427 (2000).

45 Mermin, N. D. The topological theory of defects in ordered media. *Rev. Mod. Phys.* **51**, 591 (1979).

46 Prosandeev, S. & Bellaiche, L. Asymmetric screening of the depolarizing field in a ferroelectric thin film. *Phys. Rev. B* **75**, 172109 (2007).

47 Nahas, Y. *et al.* Topology and control of self-assembled domain patterns in low-dimensional ferroelectrics. *Nat. Commun.* **11**, 5779 (2020).

48 Kornev, I., Fu, H. & Bellaiche, L. Ultrathin Films of Ferroelectric Solid Solutions under a Residual Depolarizing Field. *Phys. Rev. Lett.* **93**, 196104 (2004).

49 Hsing, G. H.-C. *Strain and Defect Engineering for Tailored Electrical Properties in Perovskite Oxide Thin Films and Superlattices*, State University of New York at Stony Brook, (2017).

50 Edwards, D. *et al.* Giant resistive switching in mixed phase $BiFeO_3$ via phase population control. *Nanoscale* **10**, 17629 (2018).

51 Ma, J. *et al.* Controllable conductive readout in self-assembled, topologically confined ferroelectric domain walls. *Nat. Nanotechnol.* **13**, 947 (2018).

52 Zhang, Q. *et al.* Deterministic Switching of Ferroelectric Bubble Nanodomains. *Adv. Funct. Mater.* **29**, 1808573 (2019).

53 Ding, L. L. *et al.* Characterization and control of vortex and antivortex domain defects in quadrilateral ferroelectric nanodots. *Phys. Rev. Mater.* **3**, 104417 (2019).

54 Rodriguez, B. J., Callahan, C., Kalinin, S. V. & Proksch, R. Dual-frequency resonance-tracking atomic force microscopy. *Nanotechnology* **18**, 475504 (2007).

55 Waghmare, U. V. & Rabe, K. M. Ab initio statistical mechanics of the ferroelectric phase transition in $PbTiO_3$. *Phys. Rev. B* **55**, 6161 (1997).

56 Zhong, W., Vanderbilt, David & Rabe, K. M. First-principles theory of ferroelectric phase transitions for perovskites: The case of $BaTiO_3$. *Phys. Rev. B* **52**, 6301 (1995).

57 Nishimatsu, T., Grünebohm, A., Waghmare, U. V. & Kubo, M. Molecular Dynamics Simulations of Chemically Disordered Ferroelectric $(Ba,Sr)TiO_3$ with a Semi-Empirical Effective Hamiltonian. *J. Phys. Soc. Jpn.* **85**, 114714 (2016).

58 Ponomareva, I., Naumov, I. I., Kornev, I., Fu, H. & Bellaiche, L. Atomistic treatment of depolarizing energy and field in ferroelectric nanostructures. *Phys. Rev. B* **72**, 140102(R) (2005).

59 Bin *et al.* Intrinsic polarization switching mechanisms in $BiFeO_3$. *Physical Review B* **95**, 104104 (2017).

60 Prokhorenko, S., Kalke, K., Nahas, Y. & Bellaiche, L. Large scale hybrid Monte Carlo simulations for structure and property prediction. *npj Comput. Mater.* **4**, 80 (2018).

61 Manton, N. & Schwarz, N. Topological solitons. *Topological Solitons, by Nicholas Manton and Paul Sutcliffe, pp. 506. ISBN 0521838363. Cambridge, UK: Cambridge University Press, July 2004.* (2004).

62 Berg, B. & Lüscher, M. Definition and statistical distributions of a topological number in the lattice O(3) σ-model. *Nucl. Phys. B* **190**, 412 (1981).

63 Kiselev, N. S. Experimental observation of chiral magnetic bobbers in B20-type FeGe. *Nat. Nanotechnol.* **13**, 451 (2018).

Acknowledgements

We thank Longqing Chen for helpful discussions. We thank Huaixun Huyan at UCI for assisting TEM experiments. This work was supported by the National Natural Science Foundation of China (Grant Nos. 0213-14380198, 11774153, 1861161004, 51672125, 51725203, 51721001, U1932115 and 11874207), National Key R&D Program of China (Grant No. 2020YFA0711504) and the Fundamental Research Funds for the Central Universities (No. 0213-14380167). Y.F.N. is supported by High Level Entrepreneurial and Innovative Talents Introduction, Jiangsu Province; C.A., X.Y, and X.Q.P. acknowledge funding from The Department of Energy (DOE) under Grant DE-SC0014430, and the NSF under grant number DMR-2034738. 4D STEM experiments was conducted using facilities and instrumentation at the UC Irvine Materials Research Institute (IMRI) supported in part by the National Science Foundation through the Materials Research Science and Engineering Center program (DMR-2011967); Researchers at the University of Arkansas acknowledge DARPA Grant No. HR0011727183-D18AP00010 (TEE Program) and the Vannevar Bush Faculty Fellowship (VBFF) Grant No. N00014-20-1-2834 from the Department of Defense. Computations were made possible thanks to the use of the Arkansas High Performance Computing Center and the Arkansas Economic Development Commission; S.C. acknowledges the support of startup grants from the Department of Applied Physics at the Hong Kong Polytechnic University, the General Research Fund (grant number 15306021) from the Hong Kong Research Grant Council, the National Natural Science Foundation of China (grant number 12104381) and the open subject of the National Laboratory of Solid State Microstructures, Nanjing University (M34001).

Author contributions

Y.F.N. conceived the idea and directed the project with X.Q.P. Y.F.C and D.W. L.H. synthesized the samples and characterized the crystalline structure with the help of Y.H.F.,H.Z.L., D.X.J and G.W. under the supervision of Y.F.N., X.Q.P. and Z.B.G. L.H. performed the PFM and CAFM measurements and data analysis with the help of H.Y.F. under the supervision of D.W. and Y.F.N.

C.A. performed 4D-STEM measurements and data analysis with the help of X.X.Y. under the supervision of X.Q.P. M.Y.W. performed SEAD and S/TEM measurements with the help of S.H.C under the supervision of P.W. and X.Q.P. S.P., Y.N., Y.Y. performed and discuss the effective Hamiltonian model simulations under the supervision of L.B. T.Q.W. helped with the lithography processing. Y.F.N. and L.H. wrote the manuscript. All authors discussed the data and contributed to the manuscript.

Competing interests

Authors declare no competing interests

Figures

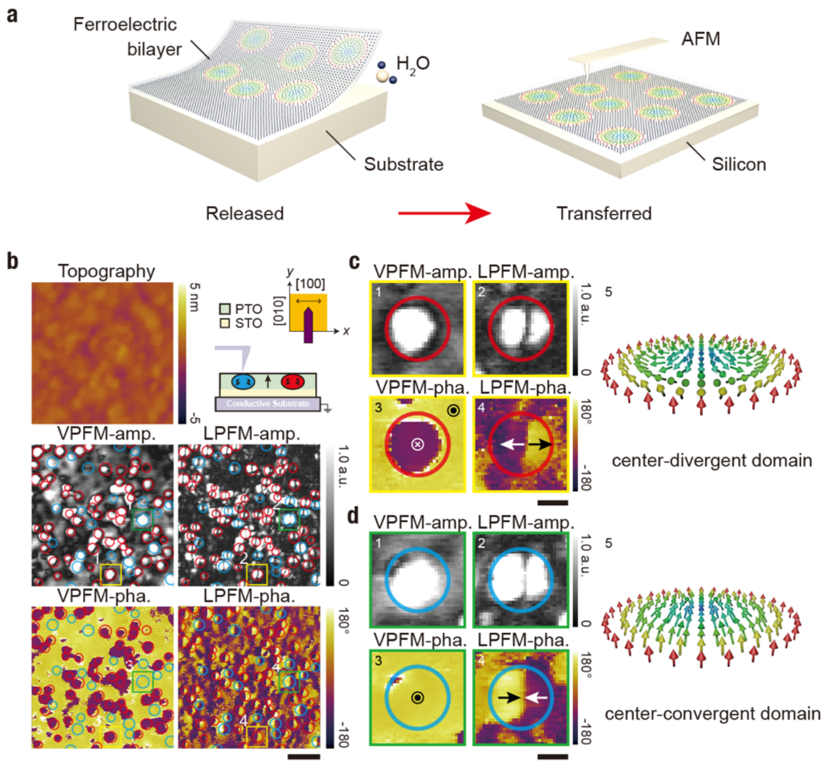

Figure 1: High-density polar nanodomains in a PTO$_{20}$/STO$_{10}$ bilayer by PFM measurements. **a,** Schematic description of the release and transfer process of oxide membranes. **b,** Topography, vertical PFM amplitude (VPFM-amp.) and phase (VPFM-pha.), lateral PFM amplitude (LPFM-amp.) and phase (LPFM-pha.) images for the freestanding PTO/STO bilayers transferred on platinized silicon substrate. Two types of topological nanodomains observed in the bilayer are marked by red and blue circles. The top right schematic drawing illustrates the sample and scan geometry showing that the cantilever is parallel to the *y* axis ([010] direction) and the contrast in the lateral PFM images reflects the *x* component of polarization vectors (along the [100] direction). All the images are from the same region. Scale bar, 100 nm. **c, d,** Zoomed-in PFM images for the two types of nanodomains: center-divergent domain (c) and center-convergent domain (d). Scale bar, 30 nm.

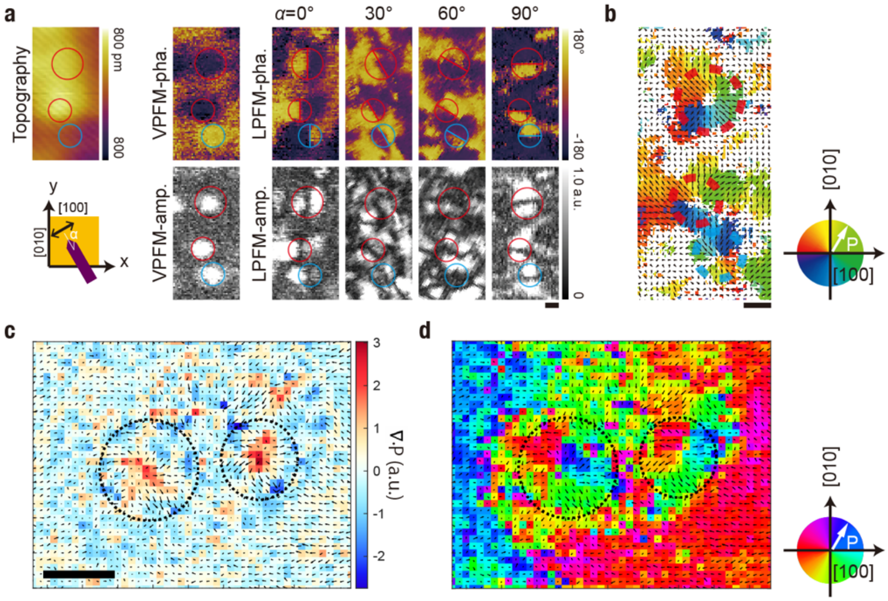

Figure 2: Polarization mapping of polar nanodomains in a PTO$_{20}$/STO$_{10}$ bilayer by vector PFM and 4D-STEM. a, Topography, lateral PFM phase and amplitude images for the same region measured with four various cantilever orientations (*α* = 0°, 30°, 60°, and 90°, where *α* is the angle between the cantilever and [010] axis). Scale bar, 30 nm. **b,** Polarization texture of the nanodomains in the same region as (a) measured by vector PFM, showing the coexistence of center-convergent and center-divergent domains that marked by dotted red and blue circles, respectively. Scale bar, 30 nm. **c, d,** Polarization mapping by 4D-STEM. Polarization mapping is calculated from conjugate pair asymmetry. Two center-divergent skyrmion-like structures are highlighted by the circles. The background in (c) shows the divergence of the polarization field. The background in (d) shows the vector direction. Scale bar, 5 nm. Note that the larger size of the nanodomains measured by PFM is most likely related to the tip size (~20 nm).

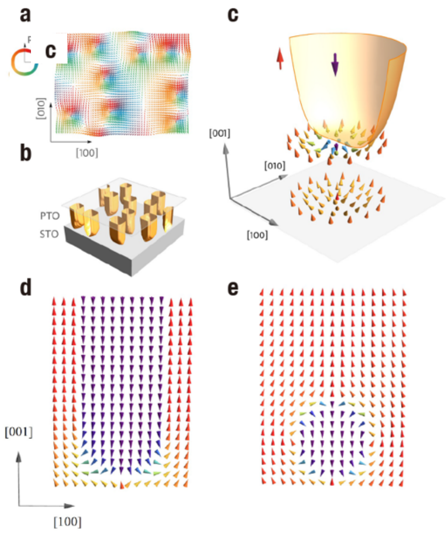

Figure 3: Effective Hamiltonian model simulations of skyrmion-like nanodomains in PTO/STO bilayers. a, The simulated in-plane polarization pattern within 50×64 u.c. part of the supercell. The arrows correspond to in-plane projection of local dipoles averaged over the bilayer thickness. **b,** The shape of simulated center-divergent nanodomains. Yellow surfaces show domain boundaries. **c,** Schematic dipolar structure of center-divergent nanodomains at the STO/PTO interface. The arrows represent dipoles in the first two layers above the interface indicated by a gray plane. **d, e,** The (010) cross-section of a typical center-divergent nanodomain (d) and a center-convergent nanodomain (e) obtained from simulations. The arrows represent unit cell dipoles colored according to their out-of-plane component.

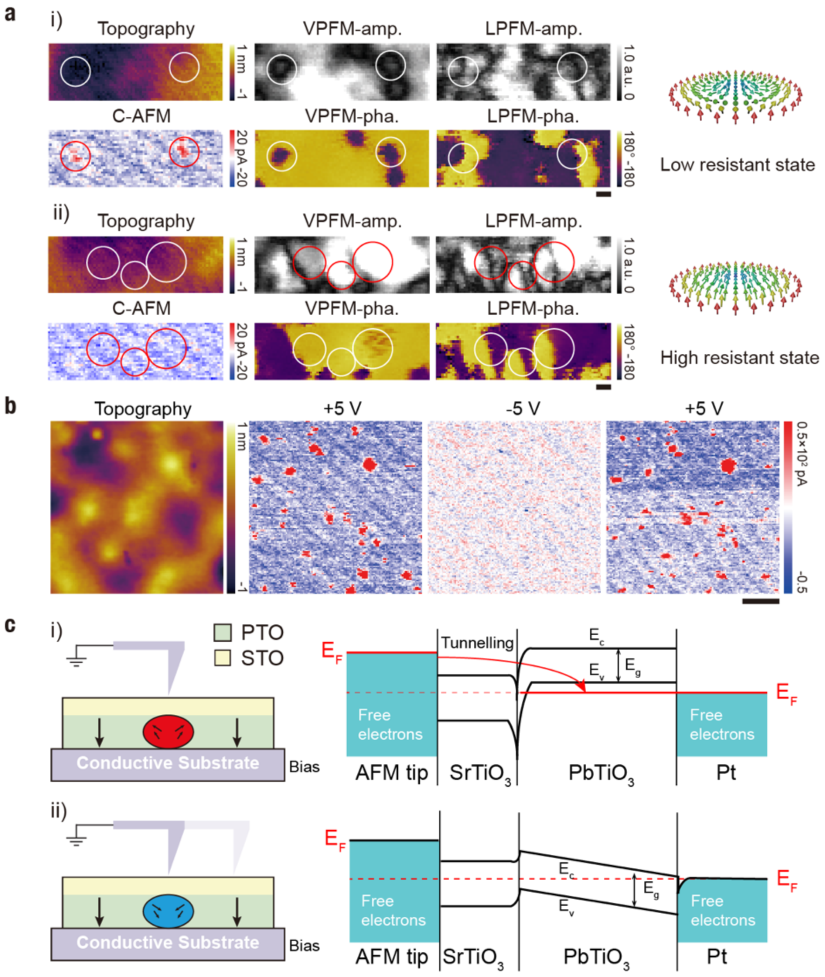

Figure 4: Polar nanodomain based resistive memories on silicon. a, Topography, vertical and lateral PFM images, and CAFM current maps collected at the same area after +5 V (i) and -5 V (ii) scan to switch the polar domains between center-divergent and center-convergent nanodomains. The CAFM images show that the center-divergent nanodomains are at low resistant state and the center-convergent nanodomains are at high resistant state. Scale bar, 20 nm. **b,** Reversible switching between the low resistant center-divergent and high resistant center-convergent states by +5 V and -5 V bias voltage. Scale bar, 50 nm. **c,** Schematic band diagram of two different types of polar structures. With significant polarization divergence near the core of the center-divergent nanodomain, hole-like charge carriers are injected, which shifts the Fermi level into the valence band. Thus, the barrier width of the junction is much narrower, resulting in a low resistive state. In contrast, due to the small polarization divergence, the center-convergent nanodomain remains at a high resistive state. (E_F, Fermi level; E_c, conduction band; E_v, valence band; E_g, bandgap).